

# Graphene bilayer Moiré lattice with Rashba spin-orbit coupling

Y. Avishai<sup>1,2</sup> and Y. B. Band<sup>1,3</sup>

<sup>1</sup>*Department of Physics, Ben-Gurion University of the Negev, Beer-Sheva, Israel.*

<sup>2</sup>*Yukawa Institute for Theoretical Physics, Kyoto, Japan.*

<sup>3</sup>*Department of Chemistry, Department of Electro-Optics,  
and The Ilse Katz Center for Nano-Science,  
Ben-Gurion University of the Negev, Beer Sheva, Israel.*

We consider twisted bilayer graphene in the presence of Rashba spin-orbit coupling and explore the physics of Moiré spintronics. The electronic charge density has a sharp step right at the magic angles  $\theta_m$ . As a result, local spin observables (polarization and equilibrium spin currents) have sharp peaks (of width about a small fraction of  $1^\circ$ ) as a function of the twist angle  $\theta$ , and abrupt sign reversals at  $\theta_m$ . Thereby, the magic angle can be determined in an unprecedented accuracy. In the first chiral limit, the spin currents vanish, but the peculiar pattern of the polarization at  $\theta_m$  persists. Major differences result in spintronics of twisted bilayer graphene at magic angles as compared with the spintronics of single and/or *un-twisted* bilayer graphene. Thus, in addition to the numerous spectacular physical phenomena already reported in twisted bilayer graphene at magic angles, new phenomena also occur in twistronic spintronics.

**Introduction:** A continuous model for exploring electronic structure of a twisted bilayer graphene that form a Moiré lattice was developed in Ref. [1] and exposed the occurrence of magic angles,  $\theta_m$ , i.e., twist angles at which the lowest energy band is relatively flat versus crystal momentum. Their origin was clarified in Ref. [2], while the symmetries and topological content of this system was analyzed in Refs. [3–5]. Recent reports have shown that this system can host correlated insulating states [6, 7], unconventional superconductivity [8], distinct Landau level degeneracies [9], emergent ferromagnetism with anomalous Hall effect and quantized anomalous Hall behavior [10–12].

Here (in addition to the spectrum), we expose the spintronic aspects of this system when it is subject to a uniform perpendicular electric field that causes Rashba spin orbit coupling (RSOC) [13] of strength  $\lambda \approx 1$  meV. The Bloch functions  $\{\Psi_{\mathbf{n}\mathbf{k}}(\mathbf{r})\}$  are evaluated and employed to calculate local spin observables [polarization and equilibrium spin currents (ESC)], as a function of the twist angle  $\theta$  (at fixed position  $\mathbf{r}$ ), at  $\varepsilon_0(\mathbf{k})$  (the lowest energy of the conduction band). On varying the twist angle  $\theta$  through a magic angle  $\theta_m$ , the density  $|\Psi_{\mathbf{n}\mathbf{k}}(\mathbf{r})|^2$  is shown to have a sharp step at magic angles  $\theta_m$  [Fig. 2(a)] and the spin observables have unusual features near  $\theta_m$  (such as narrow peaks and dips accompanied by abrupt sign changes). Specifically: (1) The polarizations  $S_x$  and  $S_y$  have sharp peaks (of width  $\approx 0.004^\circ$ ) centered at  $\theta_m$  see Fig. 3. Measuring polarization (and density) can serve as an excellent tool for determining  $\theta_m$ . (2) The planar components of the ESC  $J_{xx}$ ,  $J_{yy}$ ,  $J_{xy}$  and  $J_{yx}$  display sharp peaks and undergo an abrupt sign change at  $\theta_m$ , see Figs. 4 (note that in single layer graphene, the diagonal elements vanish [14]). (3) The symmetry  $J_{yx} = -J_{xy}$  and the equalities  $J_{xx} = J_{yy} = 0$ , valid in single layer graphene [14] are broken. (4) In the first chiral limit, the ESC vanish but the pattern of the planar polarizations  $S_x$  and  $S_y$  have both sharp peaks and sign changes at  $\theta_m$  [see Fig. 5(a)]. (5) In addition, unlike in single or double un-twisted layer graphene, all spin observables depend on the position  $\mathbf{r}$ , implying the possible occurrence of spin torque [15]. These results establish a direct link between spintronics and twistronics [16].

**Formalism:** Consider massless 2D Dirac electrons in twisted bilayer graphene (lying in the  $x$ - $y$  plane with twist angles  $\pm\theta/2$ ) subject to a uniform electric field  $\mathbf{E} = E_0\hat{z}$ . Our treatment is carried out within the continuum formulation near one of the

Dirac points, say  $\mathbf{K}'$ . The electron wave number is  $\mathbf{k} = (k_x, k_y) \in \text{BZ}$  of the (reciprocal) Moiré lattice. We denote by  $\boldsymbol{\tau}$  the isospin encoding the two-lattice structure of graphene, by  $\boldsymbol{\eta}$  the pseudo-spin operator for the two layers and by  $\boldsymbol{\sigma}$  the operator for the electron real spin. The pertinent 8 dimensional Hilbert space is then  $\boldsymbol{\eta} \otimes \boldsymbol{\sigma} \otimes \boldsymbol{\tau}$ .

**Moiré (reciprocal)  $Q$  lattice  $\mathbf{M}$ :** The reciprocal Moiré  $Q$  lattice  $\mathbf{M}$  is defined elsewhere [17] (see also Fig. 6 in Ref. [3]). Here we briefly introduce it for the sake of self-consistency. Consulting Fig. 1 and the notation of Fig. 6 of Ref. [3],  $\mathbf{M}$  is built as follows: Two-dimensional wave numbers  $\{\mathbf{Q}\}$  run over the two valleys,  $\mathbf{K}$  ( $\mathbf{Q}_r$ ) and  $\mathbf{K}'$  ( $\mathbf{Q}_b$ ) points of the hexagonal lattice. Adjacent points of different colors are connected by three vectors  $\{\mathbf{q}_j\}$ .  $|\mathbf{q}_j| = K_D = 2k_G \sin(\theta/2)$  is the reciprocal lattice constant joining Dirac points  $\mathbf{K}$  and  $\mathbf{K}'$ , in which  $k_G$  is the reciprocal lattice constant of a single graphene sheet. The coordinates of the  $Q$  points are fixed as follows: Each point in Fig. 1 (either red or blue dot) is determined by two integers,  $(n, m)$ . Taking the  $\Gamma$  point as origin, we have  $-\infty < n < \infty$ , and  $1 \leq |m| < \infty$  in units of  $K_D$ . Straightforward calculations yield,

$$\begin{aligned} \mathbf{Q}_r &= \begin{cases} [(n - (m+1)m_2/2)\sqrt{3}, \frac{1}{2}(3m-1)] & (m > 0), \\ [(n - m_2/2)\sqrt{3}, \frac{1}{2}(3m+2)] & (m < 0). \end{cases} \\ \mathbf{Q}_b &= \begin{cases} [(n - m_2/2)\sqrt{3}, \frac{1}{2}(3m-2)] & (m > 0), \\ [(n - (m+1)m_2/2)\sqrt{3}, \frac{1}{2}(3m+1)] & (m < 0), \end{cases} \end{aligned} \quad (1)$$

where  $m_2 \equiv \text{mod } 2$ . In principle, all points  $\{\mathbf{Q}\}$  are coupled in the eigenvalue problems introduced below. Practically, a reasonable cutoff in the Moiré reciprocal lattice is  $|\mathbf{Q} - \Gamma| \approx 6K_D$ , see the circle in Fig. 1. This choice keeps the symmetries studied in Ref. [4]. There are 50 red points  $\mathbf{Q}_r$  and 50 blue points  $\mathbf{Q}_b$  inside the circle. Multiplying the number of points (100) by the space dimension (8) result in Hamiltonian matrix of dimension  $N=800$ . Below we will use  $c = r, b$  to specify color. The reciprocal triangular lattice composed solely of points  $\{\mathbf{Q}_c\}$  is denoted as  $M_c$ .

**Inclusion of RSOC and the Hamiltonian:** RSOC is introduced using an  $\text{SU}(2)$  vector potential,

$$\mathbf{A} = [\boldsymbol{\sigma} \times \hat{\mathbf{z}}]. \quad (2)$$

The Hamiltonian in  $\mathbf{r}$  space,  $H = H_0(\mathbf{r}) + H_1$ , with

$$\begin{aligned} H_0(\mathbf{r}) &= \eta_0 \otimes [-i\sigma_0\partial_{\mathbf{r}} + \lambda\mathbf{A}] \cdot \boldsymbol{\tau} \\ &\quad - \frac{\theta}{2}\eta_z [(-i)\sigma_0\partial_{\mathbf{r}} + \lambda\mathbf{A}] \times \boldsymbol{\tau}, \\ H_1 &= \eta^- \sigma_0 T^\dagger + \eta^+ \sigma_0 T, \end{aligned} \quad (3)$$

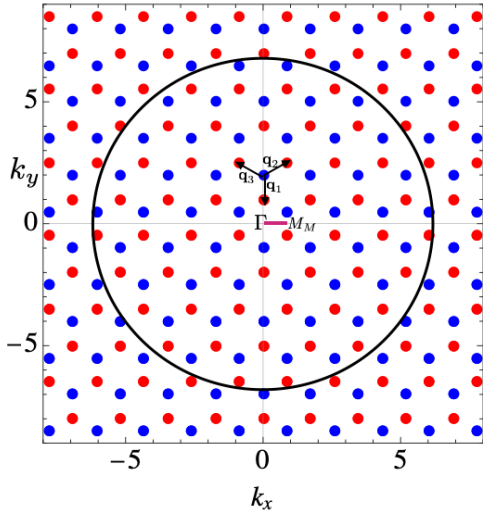


FIG. 1. Moiré reciprocal  $\mathbf{Q}$  lattice. The distance between two adjacent points is  $K_D$  and the cutoff [marked by a circle of radius  $6K_D$  centered at the  $\Gamma$  point], includes 50 red points  $\mathbf{Q}_r \in M_r$  and 50 blue points  $\mathbf{Q}_b \in M_b$ . Referring to Eq. (1), at the  $\Gamma$  point,  $(m, n) = (0, 0)$ . The three vectors  $\{\mathbf{q}_j\}$  determine the “nearest neighbor” coupling between the two layers, see Eq. (7). The spectrum in Fig. 2 is shown for  $\mathbf{k} \in \mathcal{K} \equiv [0 \leq k_x \leq k_D \frac{\sqrt{3}}{2}, k_y = 0]$ , joining the  $\Gamma$  and  $M_M$  points (bold violet segment). For twist angles around  $1^\circ$ ,  $K_D = 0.262726 \text{ (nm)}^{-1}$ . Spin observables are calculated for  $(k_x = 0.05, k_y = 0) \in \mathcal{K}$ .

is the extension of the Hamiltonian introduced in Eq. (1) of Ref. [4], with RSOC included. Here  $\lambda$ , which is proportional to  $E_0$ , is the RSOC strength, and  $T$  is a  $2 \times 2$  matrix in  $\boldsymbol{\tau}$  space (see below).

**Hamiltonian in the Bloch basis:** Recall that  $\mathbf{k} \in \text{BZ}$  is the Moiré lattice wave number, and denote by  $\mathbf{p}_c = \mathbf{k} - \mathbf{Q}_c$ , the shifted wave numbers with  $\mathbf{Q}_c \in M_c$ , ( $c = r, b$ ). Basis eigenfunctions of  $H_0(\mathbf{r})$  are  $e^{i\mathbf{p}_c \cdot \mathbf{r}} v_i(\mathbf{p}_c)$ , where  $\{v_i(\mathbf{p}_c), (i = 1, 2, \dots, 8)\}$  are the eight dimensional eigenvectors of the  $8 \times 8$  matrix obtained after replacing  $-i\partial_{\mathbf{r}} \rightarrow \mathbf{p}_c$  in Eq. (3). The corresponding energies are  $\epsilon_i(\mathbf{p}_c)$ . Putting together these eight column eigenvectors defines an  $8 \times 8$  eigenvector matrix  $\mathbf{v}(\mathbf{p}_c)$ . Both  $v_i(\mathbf{p}_c)$  and  $\epsilon_i(\mathbf{p}_c)$  are expressible analytically. A Bloch eigenfunction of  $H$  (an 8 dimensional vector), is expanded in plane-wave spinors  $\{e^{-i\mathbf{Q}_c \cdot \mathbf{r}} \mathbf{w}(\mathbf{p}_c)\}$  [defined in Eq. (4)] as,

$$\Psi_{\mathbf{k}}(\mathbf{r}) = \frac{e^{i\mathbf{k} \cdot \mathbf{r}}}{\sqrt{A}} [u_{r,\mathbf{k}}(\mathbf{r}) + u_{b,\mathbf{k}}(\mathbf{r})],$$

$$u_{c,\mathbf{k}}(\mathbf{r}) = \sum_{\mathbf{Q}_c \in M_{\mathbf{Q}_c}} e^{-i\mathbf{Q}_c \cdot \mathbf{r}} \underbrace{\left[ \sum_{i=1}^8 a_i(\mathbf{p}_c) v_i(\mathbf{p}_c) \right]}_{\mathbf{w}(\mathbf{p}_c)}, \quad (4)$$

where  $A$  is the area of a unit cell (Moiré hexagon) in position space, and  $\{a_i(\mathbf{p}_c)\}$  are  $N$  (yet unknown) coefficients. The functions  $\{u_{c,\mathbf{k}}(\mathbf{r})\}$  are dimensionless, and periodic on their respective triangular (Bravais) lattices in  $\mathbf{r}$  space. The Bloch functions  $\{\Psi_{\mathbf{k}}(\mathbf{r})\}$  and the coefficients  $\{a_i(\mathbf{p}_c)\}$  should carry also a band number  $n$  that is occasionally omitted for convenience.

Two notational definitions are useful: (1) The 100  $8 \times 8$  matrices  $\{\mathbf{v}(\mathbf{p}_c)\}$ , are used to form an  $N \times N$  block diagonal matrix

$$V \equiv \text{diag} \underbrace{[\mathbf{v}(\mathbf{p}_c)]}_{8 \times 8}, \quad \mathbf{p}_c = \mathbf{k} - \mathbf{Q}_c, \quad \mathbf{Q}_c \in M_c. \quad (5)$$

(2) The  $N$  unknown coefficients on the RHS of Eq. (4) are arranged to form a vector (of  $N$  components)  $\mathbf{a} \equiv \{a_i(\mathbf{p}_c)\}$ , where  $i = 1, \dots, 8$ .

The eigenvalue equation for the vector  $\mathbf{a}$ , employs the Bloch representation of the Hamiltonian in the presence of RSOC:

$$\begin{aligned} \mathcal{H} \mathbf{a}_n(\mathbf{k}) &= \varepsilon_n(\mathbf{k}) \mathbf{a}_n(\mathbf{k}), \\ \mathcal{H}_{\mathbf{Q}, \mathbf{Q}'} &= V^\dagger H_{\mathbf{Q}, \mathbf{Q}'} V, \\ H_{\mathbf{Q}, \mathbf{Q}'} &= \frac{1}{A} \int e^{-i\mathbf{Q} \cdot \mathbf{r}} H(\mathbf{r}) e^{i\mathbf{Q}' \cdot \mathbf{r}} d\mathbf{r}. \end{aligned} \quad (6)$$

Each element  $H_{\mathbf{Q}, \mathbf{Q}'}$  is an  $8 \times 8$  matrix in  $\boldsymbol{\eta} \otimes \boldsymbol{\sigma} \otimes \boldsymbol{\tau}$  (pseudospin-spin-isospin space), so the Hamiltonian matrix has dimension  $N \times N$  ( $N = 100 \times 8 = 800$ ). We decompose  $H_{\mathbf{Q}, \mathbf{Q}'} = H_{\mathbf{Q}, \mathbf{Q}}^0 + H_{\mathbf{Q}, \mathbf{Q}'}^1$  as follows:

$$\begin{aligned} H_{\mathbf{Q}, \mathbf{Q}}^0(\mathbf{k}) &= \eta_0 \otimes [\sigma_0 \mathbf{p} + \lambda \mathbf{A}] \cdot \boldsymbol{\tau} \\ &\quad - \frac{1}{2} \theta \zeta_{\mathbf{Q}} \delta_{\mathbf{Q}, \mathbf{Q}'} \eta_z \otimes [\sigma_0 \mathbf{p} + \lambda \mathbf{A}] \times \boldsymbol{\tau} \\ H_{\mathbf{Q}, \mathbf{Q}'}^1(\mathbf{k}) &= \eta^- \otimes \sigma_0 T_{\mathbf{Q}, \mathbf{Q}'}^\dagger + \eta^+ \otimes \sigma_0 T_{\mathbf{Q}, \mathbf{Q}'}, \\ T_{\mathbf{Q}, \mathbf{Q}'} &= \sum_{j=1}^3 [\delta_{\mathbf{Q}-\mathbf{Q}', \mathbf{q}_j} + \delta_{\mathbf{Q}'-\mathbf{Q}, \mathbf{q}_j}] T_j \\ \mathbf{q}_j &= K_D \left[ \cos \frac{(4j-3)\pi}{6} \hat{\mathbf{x}} + \sin \frac{(4j-3)\pi}{6} \hat{\mathbf{y}} \right], \\ T_j &= w_0 \tau_0 + w_1 \left[ \cos \frac{2\pi(j-1)}{3} \tau_x + \sin \frac{2\pi(j-1)}{3} \tau_y \right], \end{aligned} \quad (7)$$

which is the extension of Eq.(A3) in Ref. [4]. In  $H_{\mathbf{Q}, \mathbf{Q}}^0(\mathbf{k})$  the color index is omitted from  $\mathbf{Q}$  and  $\mathbf{p}$ , and  $\zeta_{\mathbf{Q}} = 1$  for  $\mathbf{Q}_r$  and  $-1$  for  $\mathbf{Q}_b$ . In  $H_{\mathbf{Q}, \mathbf{Q}'}^1(\mathbf{k})$  the two wave numbers have *different colors*. As far as the spectrum is concerned, diagonalization of  $H_{\mathbf{Q}, \mathbf{Q}'}$  is sufficient. For calculating wave functions, the eigenvectors  $\{\mathbf{a}\}$  are required from the solution of the first of Eq. (6), to be used in Eq. (4).

**Results:** The spectrum  $\{\varepsilon_n(\mathbf{k})\}$  depends on the potential parameters  $w_0, w_1, \theta, \lambda$ . It is calculated on the segment  $\mathbf{k} \in \mathcal{K} \equiv [0 \leq k_x \leq k_D \frac{\sqrt{3}}{2}, k_y = 0]$ , joining the  $\Gamma$  and  $M_M$  points in the Moiré  $\mathbf{Q}$  lattice (see Fig. 1(b) in Ref. [3]). The spin observables depend on  $\mathbf{k}$  and, (unlike the case of un-twisted layers), on the position  $\mathbf{r} = (x, y)$  in the unit cell (due to the presence of the coupling matrices  $\{T_j\}$ ). We use the following parameters:  $k_G = 15.0533 \text{ (nm)}^{-1}$  [2],  $w_0 = 77.0371 \text{ meV}$ ,  $w_1 = 110.053 \text{ meV}$ ,  $\lambda = 1.0544 \approx 1 \text{ meV}$  (see Ref. [20]). For twist angles around  $1^\circ$ ,  $K_D = 2k_G \sin \frac{\theta}{2} \approx 0.262726 \text{ (nm)}^{-1}$ . The spin observables are calculated for fixed  $\mathbf{k} = (k_x, k_y) = (0.05, 0) \text{ (nm)}^{-1}$ , just to the right of the  $\Gamma$  point (recall that on the  $\Gamma$  point the spin observables vanish), and at  $\mathbf{r} = 0$ , (the center of the graphene unit cell).

Our first task is to find the magic angle  $\theta_m$ . There are different criteria for its determination, such as vanishing of the Dirac speed, minimal bandwidth, or maximal band gap to higher bands. Minimal bandwidth means: Let  $\varepsilon_0(\mathbf{k}, \theta) > 0$  denote the lowest conduction band energy for  $\mathbf{k} \in \mathcal{K}$ . Then  $\theta_m$  is the twist angle that minimizes the difference

$$d(\theta) \equiv \underbrace{\{\text{Max}[\varepsilon_0(\mathbf{k}, \theta)] - \text{Min}[\varepsilon_0(\mathbf{k}, \theta)]\}}_{\mathbf{k} \in \mathcal{K}}.$$

Here we suggest yet another criterion:  $\theta_m$  is the twist angle at which the density  $|\Psi_{0\mathbf{k}}(\mathbf{r})|^2$  displays a sharp step [as in Fig. 2(a)], and, consequently, spin observables have narrow peaks and/or undergo a steep sign change [as in Fig. 3 for polarizations and Figs. 4(a,b) for ESC]. These criteria yield  $\theta_m = 1.0983^\circ$  for which  $d(\theta_m) \approx 0.098 \text{ meV}$ . The spectrum of several levels above and below the flat band is plotted in Fig. 2 when RSOC is present. In this figure  $\lambda \approx 10 \text{ meV}$  is intentionally taken to be an order of magnitude larger than realistic values in order to make the SO splitting clearly visible. For the parameters specified above, and wave number

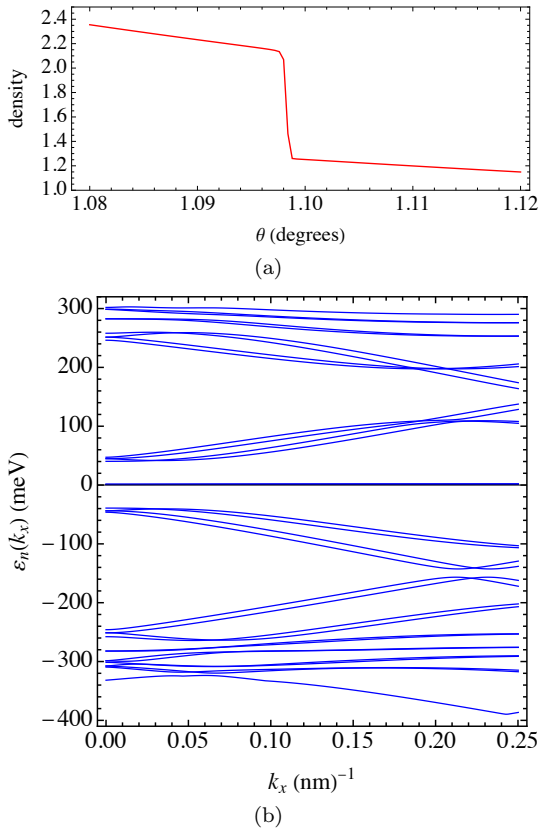


FIG. 2. (a) Dimensionless Bloch function density  $A|\Psi_{0\mathbf{k}}(\mathbf{0})|^2$  for  $\mathbf{k} = (0.05, 0) \text{ (nm)}^{-1}$  and  $\lambda = 1 \text{ meV}$  showing a step at  $\theta_m = 1.0983^\circ$  (A similar step with the same  $\theta_m$  occurs also for  $\lambda = 0$ ). (b) Low energy spectrum of twisted bilayer graphene at  $\theta_m$  for  $\mathbf{k} \in \mathcal{K}$  in the presence of RSOC. Here  $\lambda \approx 10 \text{ meV}$  is intentionally enlarged so that the SO splitting is clearly visible. As  $\lambda \rightarrow 0$ , the RSOC splitting shrinks and the level pattern is identical with that of Fig. 1(d) in Ref. [3]. The bandwidth at  $\varepsilon = 0$  is  $0.098 \text{ meV}$ , and the gap to the next band is  $\approx 43 \text{ meV}$ .

$\mathbf{k} = (0.05, 0) \text{ (nm)}^{-1}$ , the four lowest energy levels in the conduction band are  $[1.33006, 1.33006, 1.32825, 1.32825] \text{ meV}$  (i.e., they are composed of two pairs of degenerate levels). However, compared with the RSOC energy strength  $\lambda \approx 1 \text{ meV}$ , the spacing between the two pairs is very small (a few  $\mu\text{eV}$ ). Hence, one can regard them as four degenerate levels.

**Spin operators and spin observables:** Our main goal is to elucidate the spintronics of twisted bilayer graphene. This requires calculation of *local* spin observables in terms of Bloch functions, defined in Eqs. (4)-(7). Spin operators  $\hat{o}$  are  $8 \times 8$  matrices in  $\boldsymbol{\eta} \otimes \boldsymbol{\sigma} \otimes \boldsymbol{\tau}$  space. In case of  $m$ -fold degeneracy, the  $m$  degenerate eigenfunctions contribute *incoherently* to the *local* spin observables  $\{O(\mathbf{r})\}$ , (specifically, spin polarization and ESC). Explicitly,

$$O(\mathbf{r}) = \frac{1}{m} \sum_{n=1}^m \Psi_{\mathbf{k}n}^\dagger(\mathbf{r}) \hat{o} \Psi_{\mathbf{k}n}(\mathbf{r}), \quad (8)$$

where the Bloch functions are defined in Eq. (4).

**Polarization:** First, consider the polarization, for which the pertinent operator to be inserted in Eq. (8) is,

$$\hat{\mathbf{s}} = \frac{1}{2} \hbar \eta_0 \otimes \boldsymbol{\sigma} \otimes \tau_0. \quad (9)$$

As shown in Fig. 3, the planar polarizations  $S_x$  and  $S_y$  have very sharp dips at  $\theta_m = 1.0983^\circ$  (this angle was used in evaluating the spectrum in Figure 2). It is remarkable (and experimentally important) to note that for  $\lambda \approx 1 \text{ meV}$ , the polarization reaches about  $0.50\hbar$ . Away from  $\theta_m$ ,  $S_x$  and  $S_y$  are almost

constant with  $\theta$ . (The perpendicular polarization  $S_z$  vanishes identically).

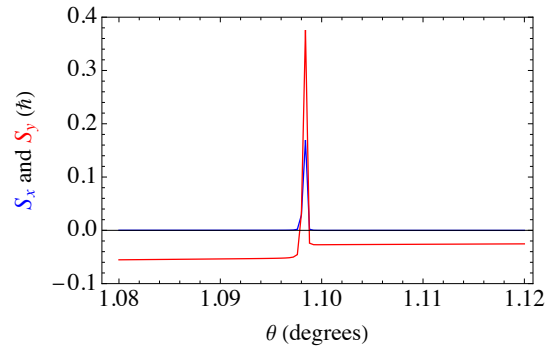


FIG. 3. Planar polarizations  $S_x$  and  $S_y$  [defined in Eqs. (9) and Eq. (8)], in the lowest positive energy state for  $(k_x, k_y) = (0.05 \text{ nm}^{-1}, 0)$  (i.e., to the right of the  $\Gamma$  point) versus twist angle  $\theta$ . The sharp peaks (of width  $\approx 10^{-4}$  degrees) determine the magic angle  $\theta_m = 1.0983^\circ$ , which is then used to compute the spectrum plotted in Fig. 2.

**Equilibrium spin current:** Here, in addition to the spin operator  $\hat{\mathbf{s}}$ , we need to introduce also the Dirac velocity operator  $\hat{\mathbf{v}} = \eta_0 \otimes \sigma_0 \otimes \boldsymbol{\tau}$ . The spin current (tensor) operator is,

$$\mathbb{J}_{ij} = \frac{1}{2} [\hat{s}_i \hat{v}_j + \hat{v}_j \hat{s}_i], \quad (i = x, y, z, \quad j = x, y), \quad (10)$$

which needs to be inserted into Eq. (8) in order to calculate the observed ESC,  $J_{ij}$ . The perpendicular components vanish,  $J_{zx} = J_{zy} = 0$ , but the planar components are finite. The diagonal planar components  $J_{xx}, J_{yy}$ , are plotted in Fig. 4(a), while the non-diagonal planar components,  $J_{xy}$  and  $J_{yx}$  are plotted in Fig. 4(b). The steep sign reversal occurs at the same angle  $\theta_m = 1.0983^\circ$ , for which the polarizations have dips. In single layer graphene [14] it is found that  $J_{xx} = J_{yy} = 0$  and  $J_{xy} = -J_{yx}$ . Here, these relations and symmetries are broken.

**Chiral limits:** References [2-5] showed that in the continuous model of twisted bilayer graphene there is an approximate anti-unitary particle-hole symmetry operator  $\mathcal{P}$  that becomes almost exact in the

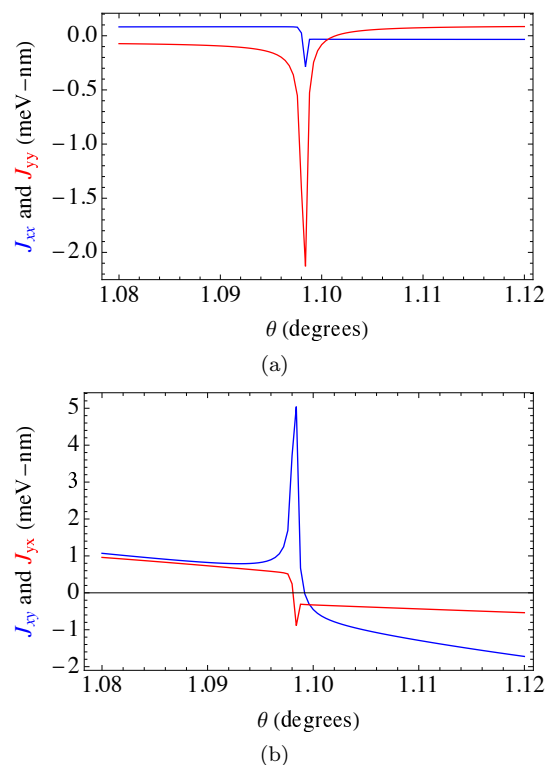


FIG. 4. Spin currents in the lowest (positive) energy state for  $(k_x, k_y) = (0.05 \text{ nm}^{-1}, 0)$  (to the right of the  $\Gamma$  point), are shown as function of the twist angle  $\theta$ . (a)  $J_{xx}$  and  $J_{yy}$ . (b)  $J_{xy}$  and  $J_{yx}$ . Sharp peaks occur at  $\theta_m = 1.0983^\circ$ , accompanied by steep sign changes.



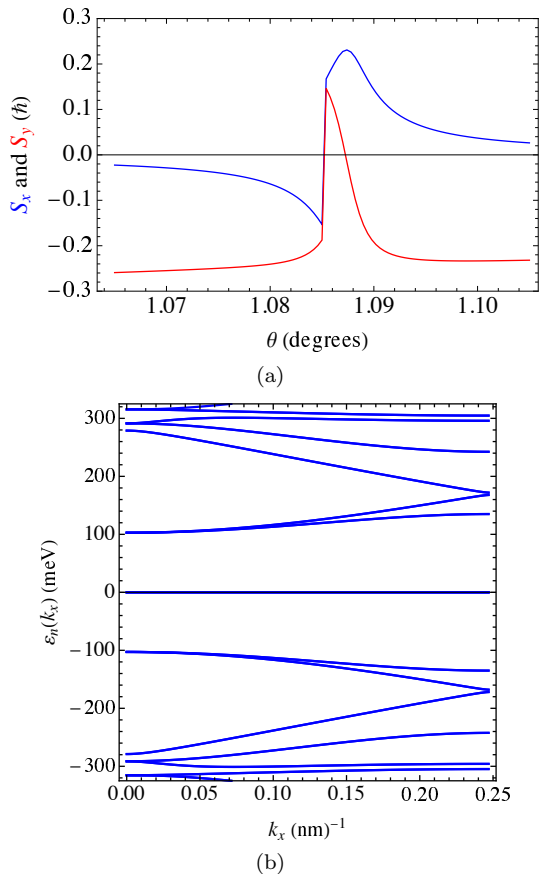


FIG. 5. Results in the first chiral limit. (a) Polarizations  $S_x$  and  $S_y$  in the chiral limit  $w_0 \rightarrow 0$  for  $\mathbf{k} = (0.05, 0) \text{ (nm)}^{-1}$ . Other parameters are as in Fig. (4). This pattern predicts a magic angle  $\theta_m = 1.0845^\circ$ . (b) The magic angle  $\theta_m$  is then used in calculating the spectrum at  $\lambda = 0$  leading to a flat band at zero energy of width 0.01 meV, and hence, particle hole symmetry is almost exact. For  $\lambda = 1 \text{ meV}$  there will be a small SO splitting that is invisible on this scale.

(so called first chiral limit),  $w_0 \rightarrow 0$ . In the presence of RSOC, it is anticipated that this operator satisfies,  $\mathcal{P}H(\mathbf{k}, \lambda)\mathcal{P}^{-1} \approx -H(-\mathbf{k}, -\lambda)$ , where the matrix elements of  $H(\mathbf{k}, \lambda)$  are given in Eq. (7). We find that in this limit, the ESC vanish, but, as shown in Fig. 5(a), the sharp peaks and steep sign reversal pattern of  $S_x$  and  $S_y$  persists, albeit at somewhat smaller magic angle. That is,  $\theta_m$  depends very weakly on  $w_0$  (here  $\theta_m = 1.0845^\circ$  while for  $w_0 = 77 \text{ meV}$ ,  $\theta_m = 1.0983^\circ$ ). Note the (almost) exact particle-hole symmetry. In the so called second chiral limit,  $w_1 \rightarrow 0$  and  $w_0 > 0$ , the system is found to be in a metal phase [3]. In particular, there is no flat band at zero energy, so it does not concern us here.

**Summary.** We explored the spin physics of electrons in twisted bilayer graphene and showed that spin observables have a remarkable behavior upon passing through a magic angle  $\theta_m$ , as illustrated in Figs. 2-5. Explicitly, for the parameters  $w_0, w_1$  used here (and elsewhere),  $\lambda \approx 1 \text{ meV}$ ,  $(k_x, k_y) = (0.05, 0) \text{ (nm)}^{-1}$ , it is found that: (1) The planar polarizations  $S_x$  and  $S_y$  have sharp dips at the magic angle, at which  $|\mathbf{S}| \approx 0.5\hbar$  (despite the small value of the RSOC strength  $\lambda \approx 1 \text{ meV}$ ). (2) The planar ESC undergo a steep sign reversal sharp peaks at the magic angle. Both properties (1) and (2) determine the magic angle  $\theta_m = 1.0983^\circ$  with very high precision. With this angle, the criteria of narrow band and large gap are convincingly satisfied, see Fig. 2(b). (3) Symmetry relations among ESC components valid in single layer [14] and untwisted bilayer graphene are broken in the twisted system. (4) Unlike in untwisted system wherein the continuous model does not impose periodicity, here,

the occurrence of the coupling matrices  $\{T_j\}$  imposes it. Hence, all spin observables depend on the position  $\mathbf{r}$ , implying the possible occurrence of spin torque [15]. But qualitatively, the pattern of spin observables described here for  $\mathbf{r} = 0$  occurs for every  $\mathbf{r}$  and at the same value  $\theta_m$ . (5) Our results pertaining to the chiral limits suggest an extension of the particle hole symmetry discussed in Refs. [3-5].

Thus, in addition to the association of magic angles with flat bands, correlated insulating states, unconventional superconductivity, ferromagnetism with anomalous Hall effect and distinct Landau level degeneracies, they are also relevant to the pertinent spin physics. Following the recent developments in the research of monolayer and (untwisted) multilayer graphene spintronics [23, 24], we expect our study of twistrionic spintronics to stimulate experimental and further theoretical work on the emergent field of Moiré spintronics. This expectation is supported by the fact that the spin observables calculated here can be measured using spin and angle-resolved photoelectron spectroscopy [25, 26] and polarized light scattering [27].

We are grateful to Rafi Bistritzer, Zhi-Da Song, Pilkyung Moon, Alex Kruchkov and Ady Stern for useful discussions.

- 
- [1] R. Bistritzer and A.H. MacDonald, Proceedings of the National Academy of Sciences **108**, 12233 (2011).
  - [2] G. Tarnopolsky, A. J. Kruchkov, and A. Vishwanath, Phys. Rev. Lett. **122**, 106405 (2019).
  - [3] Zhi-Da Song, B. Lian, N. Regnault, and B. A. Bernevig, Phys. Rev. B **103**, 205412 (2021).
  - [4] Zhi-Da Song, Zhijun Wang, Wujun Shi, Gang Li, Chen Fang, and B. Andrei Bernevig, Phys. Rev. Lett. **123**, 036401 (2019).
  - [5] B. A. Bernevig, Zhi-Da Song, N. Regnault, and B. Lian, Phys. Rev. B **103**, 205413 (2021).
  - [6] Y. Cao, V. Fatemi, A. Demir, S. Fang, S.L. Tomarken, J.Y. Luo, J.D. Sanchez-Yamagishi, K. Watanabe, T. Taniguchi, E. Kaxiras, et al. Nature **556**, 80 (2018).
  - [7] Y. Cao, J.Y. Luo, V. Fatemi, S. Fang, J.D. Sanchez-Yamagishi, K. Watanabe, T. Taniguchi, E. Kaxiras, and P. Jarillo-Herrero, Phys. Rev. Lett. **117**, 116804 (2016).
  - [8] Y. Cao, V. Fatemi, S. Fang, K. Watanabe, T. Taniguchi, E. Kaxiras, and P. Jarillo-Herrero, Nature **556**, 43 (2018).
  - [9] X. Lu, P. Stepanov, W. Yang, M. Xie, M.A. Aamir, I. Das, C. Urgell, K. Watanabe, T. Taniguchi, G. Zhang, et al., Nature **574**, 653-657 (2019).
  - [10] A. L. Sharpe, E. J. Fox, A. W. Barnard, J. Finney, K. Watanabe, T. Taniguchi, M. A. Kastner, and D. Goldhaber-Gordon, (2019). Science **365**, 605 (2019).
  - [11] J. H. Pixley, and E. Y. Andrei, Science **365**, 543 (2019).
  - [12] M. Serlin, C. L. Tschirhart, H. Polshyn, Y. Zhang, J. Zhu, K. Watanabe, T. Taniguchi, L. Balents, and A. F. Young, Science, **367**, 900 (2020).
  - [13] E. I. Rashba, Sov. Phys. Solid State **2**, 1109 (1960); Y. A. Bychkov and E. I. Rashba, JETP Lett. **39**, 78 (1984); H. A. Engel E. I. Rashba and B. I. Halperin, "Theory of Spin Hall Effects in Semiconductors", arXiv:cond-mat/0603306.
  - [14] H. Zhang, Z. Ma and J. F. Liu, Scientific Reports **4**, 6464 (2015).
  - [15] J. Shi, P. Zhang, D. Xiao, and Q. Niu, Phys. Rev. Lett. **96**, 076604 (2006).
  - [16] <https://en.wikipedia.org/wiki/Twistrionics>.
  - [17] P. Moon and M. Koshino, Phys. Rev. B **85**, 195458

- (2012); Phys. Rev. B **87**, 205404 (2013); Phys. Rev. B **90**, 155406 (2014).
- [18] M. Gmitra, S. Konschuh, C. Ertler, C. Ambrosch-Draxl, and J. Fabian, Phys. Rev. B **80**, 235431 (2009).
- [19] S. Konschuh, M. Gmitra, and J. Fabian, Phys. Rev. B **82**, 245412 (2010).
- [20] M. Gmitra and J. Fabian, Phys. Rev. B **92**, 155403 (2015).
- [21] Y.-H. Zhang, D. Mao, Y. Cao, P. Jarillo-Herrero, and T. Senthil, Phys. Rev. B **99**, 075127 (2019).
- [22] Z. Sun and Y. H. Hu, Matter **2**, 1106 (2020).
- [23] A. Avsar, H. Ochoda, F. Guinea, B. Özyilmaz, B. J. van Wees, and I. J. Vera-Marun, Rev. Mod. Phys., **92**, 021003 (2020).
- [24] K. Zollner and J. Fabian, Phys. Rev. B **104**, 075126 (2021).
- [25] C. Tusche, A. Krasyuk, J. Kirschner, Ultramicroscopy **159**, 520 (2015).
- [26] M. Unzelmann, *et al.*, Nature Communications **12**, 3650 (2021).
- [27] J. Wang, B-F Zhu, and R-B Liu, Phys. Rev. Lett. **100**, 086603 (2008).